Composites: Part A 82 (2016) 78–87

Contents lists available at ScienceDirect

Composites: Part A

journal homepage: www.elsevier.com/locate/compositesa

Molecular dynamics simulation of the nonlinear behavior of the CNT-reinforced calcium silicate hydrate (C–S–H) composite

Mehdi Eftekhari [a], Soheil Mohammadi [b,*]

[a] Department of Civil Engineering, Rasht Branch, Islamic Azad University, Rasht, Iran
[b] High Performance Computing Lab, School of Civil Engineering, University of Tehran, Tehran, Iran

ARTICLE INFO

Article history:
Received 19 June 2015
Received in revised form 3 November 2015
Accepted 30 November 2015
Available online 12 December 2015

Keywords:
A. Carbon nanotubes and nanofibers
A. Reinforced cement/plaster
B. Mechanical properties
B. Interface/interphase

ABSTRACT

Calcium–Silicate–Hydrate (C–S–H), which is the major constituent of the cement at the nanoscale, is responsible for the strength and fracture properties of concrete. This research is dedicated to the numerical study of enhanced mechanical properties of C–S–H reinforced by embedding carbon nanotube (CNT) in its molecular structure. Series of molecular dynamics (MD) simulations indicate that the tensile strength of CNT-reinforced C–S–H is substantially enhanced along the direction of CNT as compared to the pure C–S–H. The results of tensile loading reveal that CNT can efficiently bridge the two sides of cracked C–S–H. In addition, CNTs can severely intensify the "transversely isotropic" response of the CNT-reinforced C–S–H. Furthermore, the pull-out behavior of CNT reveals that the force-displacement response can be estimated by a bilinear model, which can later be used for simulation of cohesive crack propagation and multiscale simulation of crack bridging at macro scale specimen of CNT-reinforced cement.

1. Introduction

Nowadays, there is an increased demand for production of high strength and more efficient types of material in construction industry. Due to its multiscale nature and composition, properties of concrete, as one of the most common construction materials, depend on many factors. It is composed of different amorphous phases ranging from nanometer to millimeter sizes. Damage and degradation of concrete occur across different length scales, and the properties of the coarser scale rely on the finer ones. One of the most important components of concrete, which plays a significant role in its mechanical properties, is the cement. Enhancing the properties of the cement could lead to the overall improvement of the concrete behavior.

Cement usually exhibits brittle behavior in tension and compression. Brittleness of cement can be modified by implementation of traditional steel reinforcing bars and random distribution of steel and polymeric fibers for preventing or containing propagation of macro and micro cracks. In contrast to conventional reinforcing materials, nowadays, nanomaterial additives in cement allow for improving the tensile strength, creep behavior, resistance to impact loading of concrete specimen [1] and preventing progressive crack propagation [2]. Carbon nanotubes/nanofibers (CNTs/CNFs) with high strengths in tension and compression [3], high modulus of elasticity and excellent mechanical properties, are increasingly attractive nano additives for cement-based composites [2].

While applications of CNTs have been comprehensively studied in polymeric-based composites [4,5], only limited number of researches have addressed their effects on cement. For instance, Cwirzen et al. [6] indicated that addition of CNTs to the cement paste improved the workability and increased the compressive strength up to 50%. In addition, pristine CNTs could improve the flexural and compressive strength of the cement about 10–20% [7]. Also, numerical investigation of Eftekhari et al. [1,2] revealed that addition of CNTs to the cement could significantly increase the fracture energy and tensile strength of the CNT-reinforced cement and delay the crack propagation.

To improve the mechanical behavior of cement, it is essential to investigate the properties of the nanogranular binding phase of the cement and to optimize its mechanical properties at the finer scales, especially by CNTs at the nano and atomic scales. Cement is made of hydrated and unhydrated products in a porous medium. The strength of the cement is largely affected by the hydration products [8]. The major component of the hydrated products,

* Corresponding author at: College of Civil Engineering, University of Tehran, Enghelab Ave., Tehran, Iran.
E-mail addresses: mehdi_eft@yahoo.com (M. Eftekhari), smoham@ut.ac.ir (S. Mohammadi).

http://dx.doi.org/10.1016/j.compositesa.2015.11.039
1359-835X/

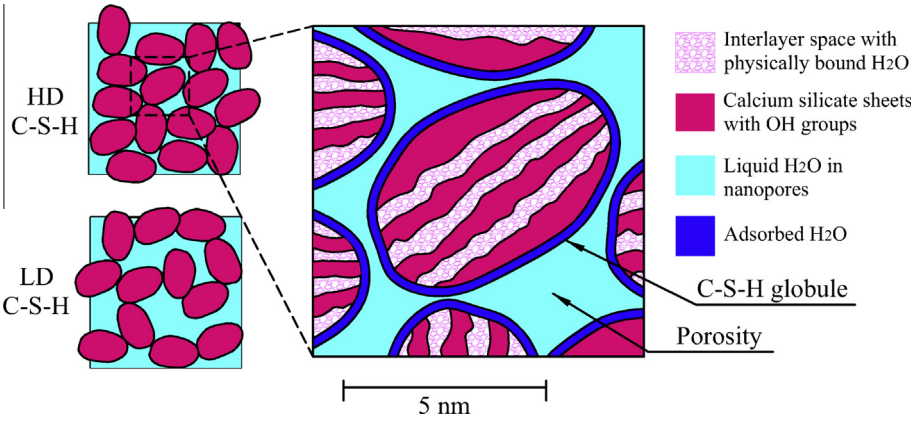

Fig. 1. Typical nano structure of C–S–H [4]. (For interpretation of the references to colour in this figure legend, the reader is referred to the web version of this article.)

which constitutes 60–70% volume fraction of the hydrated cement and plays a significant role on its mechanical properties, is a nanogranular rigid gel, called the Calcium–Silicate–Hydrate (C–S–H) [9]. Several models have been suggested and developed for C–S–H [10–15]. For the first time, Powers and Brownyard [13] proposed a colloidal gel-like structure for C–S–H, which was later examined by Tennis and Jennings [15]. Taylor [14] proposed that the nano structure of C–S–H is an imperfect layered hybrid of two types of crystalline minerals, namely, Tobermorite and Jennite.

It is believed that C–S–H is the elementary building block of the cement and is made of aggregation of 5 nm brick-shape nanoparticles, called "globules", which form a nanoporous gel-like network [16] (Fig. 1). These globules of C–S–H form the overall structure of the cement paste and are responsible for its mechanical properties such as cohesion and strength. During the hydration of cement, C–S–H globules form two types of gel with different mechanical properties and low (LD) and high (HD) packing densities, which have 37% and 24% gel porosities, respectively. HD C–S–H has higher strength and stiffness [15]. The volume fraction ratio of LD and HD C–S–H changes according to the water to cement ratio in different cements. At the atomic level, C–S–H has a layered structure, composed of short silicate chains attached together by calcium oxide, with the water inside the structure [17] (Fig. 1). The structure of C–S–H is usually defined by the molar ratio of calcium to silicon ratio, which correlates well with the mechanical properties of C–S–H and depends on the water/cement ratio. This parameter varies in the range of 0.6–2.3 with a mean value of 1.7 [16].

Recently, several authors have studied the mechanical properties and atomic structure of C–S–H by the molecular dynamics (MD) approach. Among them are Manzano et al. [18] who investigated the effect of the composition (such as Ca/Si and Water/Ca ratios) and length of silicate chains on the bulk, shear and Young's modulus of C–S–H by means of different forms of interatomic potential. They found that only a little decline in the mechanical properties would be observed when the Ca/Si ratio and the number of water molecules increased. In addition, when they reduced the length of the silicate chains in the crystalline structures of C–S–H, the results were in better agreement with the experimental data. A turning point in the molecular simulation of C–S–H was the research conducted by Pellenq et al. [19]. They proposed a realistic molecular model of C–S–H, which could reasonably predict its structural and physical properties observed in experimental tests. Furthermore, the tensile and compressive behaviors of C–S–H were derived by Murray et al. [20] based on the molecular dynamics approach. Their finding indicated that the compressive and tensile strengths of C–S–H were three times higher than the cement at the macro scale. In addition, the tensile strength of C–S–H was 23% of the compressive strength. They found that electrostatic and bond forces in the silicate chains were the main factors for the strength of cement at the atomic scale. Besides, Abdolhosseini Qomi et al. [16] tried to numerically optimize the properties of cement hydrate by means of the MD method for different types of defects.

Despite the fact that several studies have been conducted on the molecular dynamics simulation of C–S–H (such as

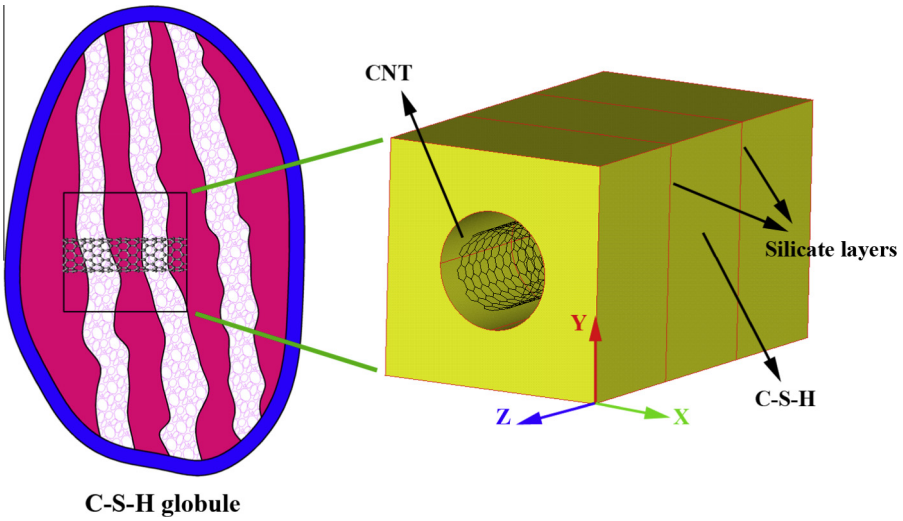

Fig. 2. The model of CNT-reinforced C–S–H. (For interpretation of the references to colour in this figure legend, the reader is referred to the web version of this article.)

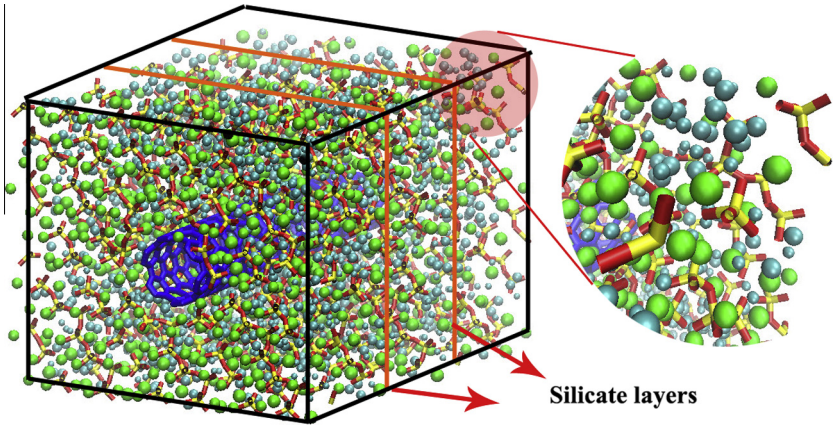

Fig. 3. The molecular structure of CNT-reinforced C–S–H phase: the red and cyan are oxygen and hydrogen atoms of water molecules, respectively; the blue is CNT, inter and intra-layer calcium ions are green; and the Silicon is demonstrated as yellow (refer to the electronic version for a better view). (For interpretation of the references to colour in this figure legend, the reader is referred to the web version of this article.)

[12,16,19,21–26]), but based on the knowledge of the authors, no published report is available on molecular dynamics study of the mechanical properties of CNT-reinforced C–S–H. The ultimate goal of the current study is to comprehensively investigate the mechanical properties of CNT-reinforced C–S–H. Therefore, a finite volume of the C–S–H globule atomistic structure containing a CNT is considered for further investigation, as depicted in Fig. 3. The periodic boundary condition is used for all directions of the simulation box [19]. Several authors have recently studied aligned-CNTs in different matrices, such as the alumina matrix composites [27,28], and It is now practically possible to produce CNT-reinforced C–S–H specimen, where CNTs are aligned in a specific direction, i.e. perpendicular to the silicate layer, which is considered in this study. The schematic structure of such CNT-reinforced C–S–H with periodic boundary conditions is depicted in Fig. 2.

The paper is organized as follows; in Section 2, the molecular structure of a CNT-reinforced C–S–H is generated based on [16], and the implemented interatomic potential are described. In Sections 3 and 4, the mechanical properties of CNT and CNT-reinforced C–S–H, including tensile, compressive and shear stress–strain curves are derived by the molecular dynamics method. Finally, the pull-out behavior of CNT is discussed in Section 5.

2. Simulation method

The initial molecular structure of C–S–H and the interatomic potential parameters are obtained from [16]. A triclinic crystal system with the periodic boundary conditions is used for simulation of C–S–H phase containing a reinforcing CNT. In the triclinic system, the crystal is described by three mutually non-orthogonal vectors (a,b,c) and the angles between vectors are defined as (α, β, γ). The lattice parameters for the C–S–H triclinic box are $a = 39.25$ Å, $b = 36.26$ Å, $c = 47.68$ Å, $\alpha = 88.97^\circ$, $\beta = 92.81^\circ$, $\gamma = 88.57^\circ$. The atomic structure of the problem is illustrated in Fig. 3.

In the current study, due to the fact that the C–S–H structure is weaker along the Z direction (perpendicular to the silicate layer) (Fig. 2), it is assumed that the CNT is aligned along the Z direction to obtain the most efficient reinforcement. The CNT-reinforced C–S–H with random orientation of CNTs is the subject of an independent study. The molecular dynamics method is adopted for simulation of the CNT-reinforced C–S–H and determining the related mechanical and structural properties. The Large-scale Atomic/Molecular Massively Parallel Simulator (LAMMPS) [29] is used for the MD simulation. 1 fs is chosen for the timestep.

The total interatomic potential energy function for the C–S–H consists of four components; the harmonic bond stretching (1), the harmonic bond angle bending (2), the Columbic interaction (3), and the Lennard-Jones (L-J) potential (4) [16]. The long range Columbic interactions are calculated based on the Wolf summation technique [30], and the cut-off radius for the L-J potential is assumed to be 12 Å:

$$E_{\text{bondstretch}} = 0.5 \times k_b \times (r_{ij} - r_0)^2 \tag{1}$$

$$E_{\text{anglebend}} = 0.5 \times k_\theta \times (\theta_{ijk} - \theta_0)^2 \tag{2}$$

$$E_{\text{Coul}} = \frac{e^2}{4\pi\varepsilon_0} \sum_{i \neq j} \frac{q_i q_j}{r_{ij}} \tag{3}$$

$$E_{L-J} = \sum_{i \neq j} \left[\frac{C_{12}}{r_{ij}^{12}} - \frac{C_6}{r_{ij}^{6}} \right] \tag{4}$$

where k_b and k_θ are force constants, r_{ij} is the interatomic distance, r_0 is the bond length at the equilibrium state, θ_{ijk} is the angle between two bonds, θ_0 is the angle at the equilibrium state, e is the charge of electron, ε_0 is the dielectric permittivity of vacuum 8.85419×10^{-12} F/m, q_i and q_j are the partial charge of the two atoms i and j and C_{12} and C_6 are the L-J constants. Values of these parameters are provided in Appendix A. In addition, the modified Tersoff interatomic potential is adopted for interaction among the carbon atoms of CNT [3].

$$E_{ij}^{\text{Tersoff}} = \frac{1}{2} f_C(r_{ij}) [f_R(r_{ij}) + b_{ij} f_A(r_{ij})] \tag{5}$$

$$f_R(r_{ij}) = A_{ij} \exp(-\lambda_{ij} r_{ij}), \quad f_A(r_{ij}) = -B_{ij} exp(-\mu_{ij} r_{ij}) \tag{6}$$

$$f_C(r_{ij}) = \begin{cases} 1, & r_{ij} \leq R_{ij} \\ \frac{1}{2} + \frac{1}{2} \cos[\pi (r_{ij} - R_{ij})/(S_{ij} - R_{ij})], & R_{ij} < r_{ij} < S_{ij} \\ 0, & r_{ij} \geqslant S_{ij} \end{cases} \tag{7}$$

where functions $f_R(r_{ij})$ and $f_A(r_{ij})$ represent the repulsive and attractive interactions, respectively. Further details about the Tersoff potential can be found in [31].

One of the main issues for simulation of this problem is the way interaction of CNT and C–S–H is handled, as it is a key factor for the load-transfer capacity, and consequently the overall macroscopic behavior of the composite. While a few number of studies have been performed to investigate the mechanical properties of several types of functionalized and non-bonded (van der Waals) groups of

graphene reinforced C–S–H [32,33], there is no report on CNT-reinforced C–S–H. Results of these studies imply that the surface functionalization can improve the interfacial interaction among C–S–H and the functionalized graphene. This paper, however, does not cover functionalized CNTs, and only the van der Waals interaction among carbon and C–S–H atoms is considered at the room temperature with atmosphere pressure [32,33]. The Lorentz–Berthelot mixing rules are adopted to evaluate the parameters of the Lennard–Jones interaction (σ, ε) for different CNT and C–S–H atoms [33],

$$\sigma_{ij} = \frac{1}{2}(\sigma_{ii} + \sigma_{jj}) \tag{8}$$

$$\varepsilon_{ij} = \sqrt{\varepsilon_{ii}\varepsilon_{jj}} \tag{9}$$

where σ and ε are the L-J parameters for i and j atoms.

Finally, among several models available for water molecules [9], the well-known simple and efficient simple point charge (SPC) model is used for simulation of water molecules [16]. In this model, the bond stretch and bond angle bending behavior between hydrogen and oxygen atoms have finite stiffness of 47.656 eV/Å^2 and 3.9362 eV/Rad^2, respectively. These atoms have partial charges and interact through the Columbic interaction. The equilibrated length and angle between the oxygen and hydrogen atoms are $r = 1$ Å and $\theta = 109.47°$, respectively.

3. Mechanical properties of CNT

Among several existing types of CNTs, only two most common types of CNTs with equal diameters (8.13 Å) and lengths (40 Å), namely, armchair (6,6) and zigzag (10,0) are considered in this study. To calculate the stress–strain curve of the CNT, one side of the CNT is constrained and the other side is moved with a constant velocity of 0.01 Å/ps, and the corresponding stress and strain values are obtained. The pressure of the simulation box is obtained and stands for the mechanical stress. This is a conventional practice used by several authors [16,19,21]. With respect to the results of [34], three different compressive strain rates are applied to evaluate the mechanical behavior of CNTs. Fig. 4. indicates that the 0.01 Å/ps strain rate, which has been used in the present study, is fair enough to remove the effects of strain rate dependency on the buckling behavior of CNTs, as similar stress–strain curves are obtained for other strain rates.

The mechanical properties of CNT (as a reinforcement material) are reported in Table 1. Clearly, CNT is a high strength material. The compressive strength of the zigzag CNT is 10% higher than the armchair one, but in the case of tensile and shear strengths, the armchair strength is superior than the zigzag CNT about 21% and 24%, respectively.

Table 1
Mechanical strengths for the CNT.

Models	Tensile strength (Gpa)	Compressive strength (Gpa)	Shear strength (Gpa)
Armchair (6,6)	126.71	95.96	18.51
Zigzag (10,0)	104.74	105.14	14.94

The tensile, compressive and shear stress–strain curves of the CNT are illustrated in Fig. 5. In Fig. 5a, one can observe that the tensile stress of CNT increases continuously until a sudden rupture in its cross section happens and the stress drops to zero. On the other hand, the compressive stress increases almost linearly before the tube buckles abruptly (Fig. 5b). Finally, the shear behavior of the CNT is almost linear, but with more fluctuation until it reaches the maximum shear capacity with a sudden decline in the shear stress (Fig. 5c).

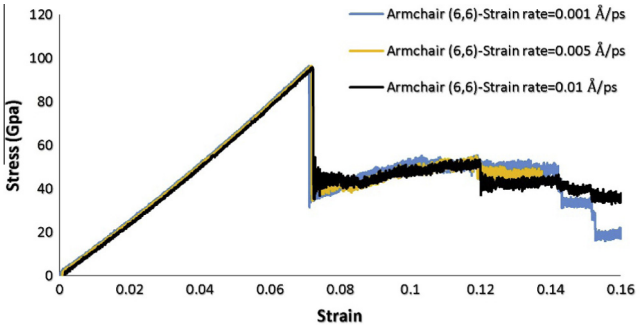

Fig. 4. Strain rate effect on the buckling behavior of CNTs. (For interpretation of the references to colour in this figure legend, the reader is referred to the web version of this article.)

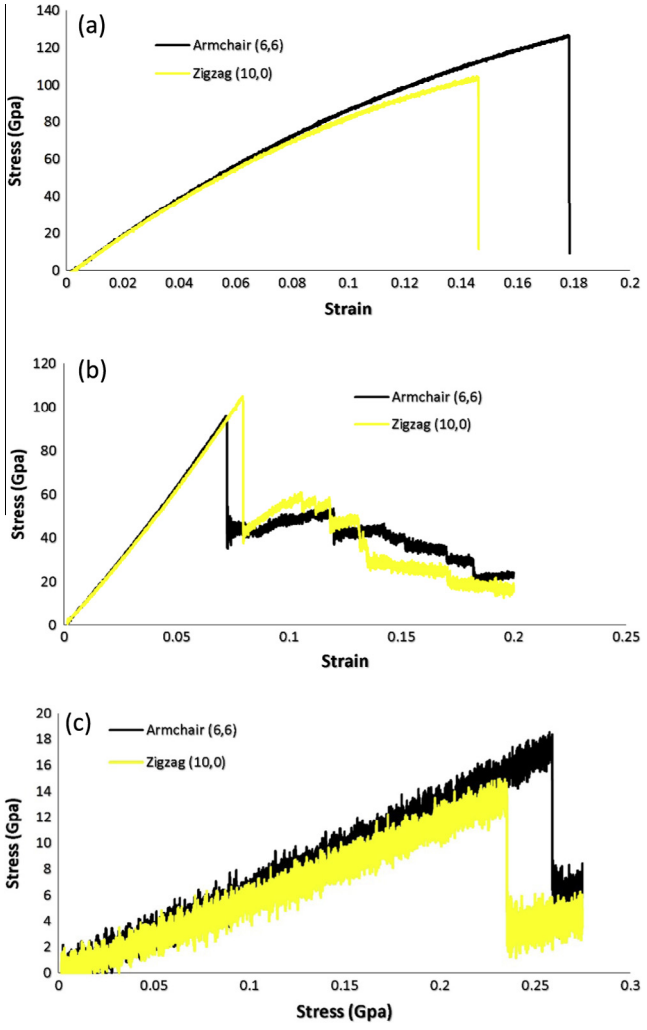

Fig. 5. Stress–strain curves of CNT, (a) tensile, (b) compressive, (c) shear. (For interpretation of the references to colour in this figure legend, the reader is referred to the web version of this article.)

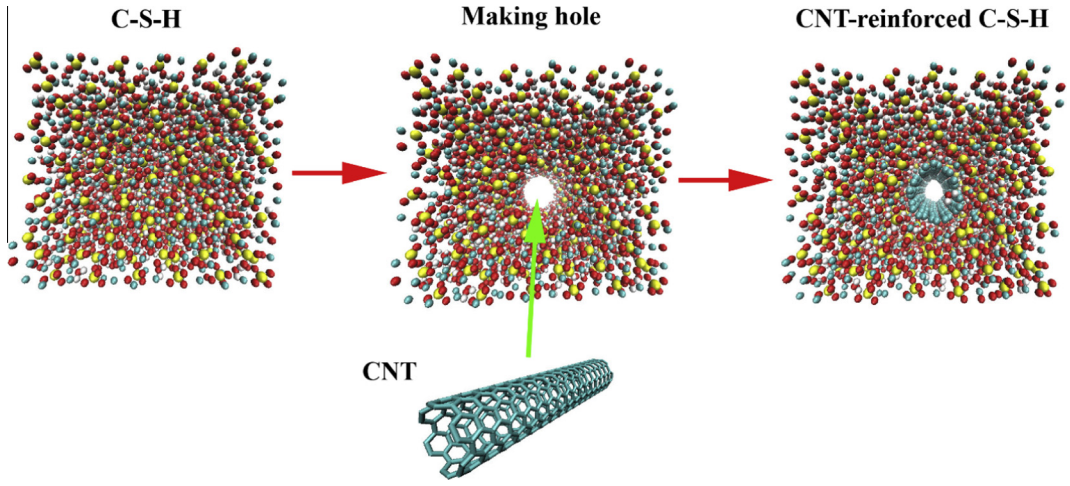

Fig. 6. Schematic representation of the construction of CNT-reinforced C–S–H. (For interpretation of the references to colour in this figure legend, the reader is referred to the web version of this article.)

4. Mechanical properties of CNT-reinforced C–S–H

In this section, three models are examined: a C–S–H box without CNT (CSH), a C–S–H box reinforced by an armchair (6,6) CNT (CSH + Armchair) and a C–S–H box reinforced by a zigzag (10,0) CNT (CSH + Zigzag). The CNT is positioned in the middle of the C–S–H box along the *Z* direction, which is perpendicular to the silicate layers. Both CNTs have a finite length of 40 Å. The Ca/Si ratio (molar ratio of $CaO–SiO_2$) of the C–S–H structure varies from 1.2 to 2.3 in calcium silicate hydrate phase [35]. In this study, the Ca/Si ratio is assumed to be 1.6. It is out of scope of the current study to investigate the effect of Ca/Si ratio.

The simulation is performed in the following procedure: because the models are in the room environment (constant pressure and temperature), first, a random velocity is applied to the initial structure of C–S–H box in order to reach to the room temperature (300 K) using an NPT ensemble with atmospheric pressure on all dimensions of the simulation box until the structure reaches an equilibrated state. The temperature is maintained at 300 K by the Nosé–Hoover thermostat. Afterwards, an energy minimization is applied to the system via the conjugate gradient algorithm to remove the residual stresses of atoms (produced by the NPT ensemble in the previous step). In the next step, a cylindrical hole is gradually indented in the center of the C–S–H box with a diameter of 12.5 Å, perpendicular to the silicate layer, in 2500 steps. The special technique of "fix indent cylinder" command of LAMMPS code is adopted to generate a zero-diameter hole. This hollow cylinder is inserted into the C–S–H with a diameter of zero and its diameter is gradually increased, pushing the atoms backwards. Consequently, no bond breaks or forms. Afterwards, the CNT is embedded in the cylindrical hole, the L-J potential between the C–S–H and CNT is activated, and the model is analyzed. It is observed that the equilibrium of the system is achieved after 300 steps (equal to 0.3 ps). The L-J interaction between the C–S–H and carbon atoms determines the equilibrated interlayer space between the CNT and C–S–H, which becomes approximately 2.7 Å. A schematic representation of the mentioned procedure for the construction of CNT-reinforced C–S–H model is depicted in Fig. 6.

Once the system is in the equilibrium state, uniaxial and shear deformations are imposed in six independent directions (axial *X*, *Y*, *Z* and shear *XY*, *XZ*, *YZ*) of the simulation box with a constant velocity of 1 Å/ps in an NVT ensemble. Accordingly, the pressure of the system is determined from the applied strain. Consequently, after full application of deformation, the corresponding stress–strain response is derived. The elastic constants of the models are calculated from the initial linear part of the obtained stress–strain curves. Since the C–S–H is a triclinic crystal, 21 independent elastic constants need to be determined.

Due to the fact that, based on the knowledge of the authors, no research has so far been performed to determine the mechanical properties of CNT-reinforced C–S–H, in the current study, a C–S–H model, previously simulated by Shahsavari et al. [21] is modeled for verification at 300_K (Fig. 7). The *X*–*Y* plane is parallel to the silicate layers and the *Z* direction is perpendicular to the silicate layers. An illustration of the simulation box is shown in Fig. 7.

The results of the components of the compliance tensor for the current C–S–H model and reference [21] are compared in Table 2. Clearly, the significant difference between the C_{33} component with C_{11} and C_{22} indicates that the properties of C–S–H is very similar to the "transversely isotropic" material (1, 2 and 3 corresponds to *X*, *Y* and *Z*, respectively). That is due to the existence of silicate layers parallel to the *XY* plane of the molecular structure (Fig. 7). We have used the most recent and sophisticated model and the interatomic potential for C–S–H nanostructure, based on the results of [16]. While Abdolhosseini Qomi et al. [16] enhanced and improved the interatomic potential and geometry of the model mentioned in Shahsavari et al. [21] in 2011, they did not provide complete results of the elastic tensor for the C–S–H model. In contrast, the earlier work by Shahsavari et al. [21] provided the complete data

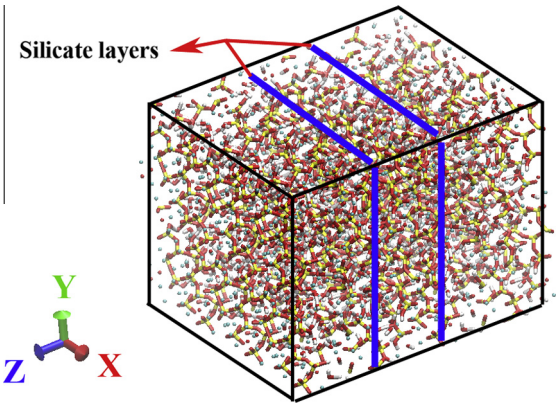

Fig. 7. Atomic structure of C–S–H phase. (For interpretation of the references to colour in this figure legend, the reader is referred to the web version of this article.)

Table 2
Components of the compliance tensor for the C–S–H specimen (Gpa).

	Shahsavari et al. [21]	Current study	Difference (%)
C_{11}	86.17	76.24	11
C_{12}	34.29	36.16	5
C_{13}	35.64	19.92	44
C_{22}	85.49	77	9
C_{23}	32.34	24	25
C_{44}	18.25	9.98	45
C_{55}	17.71	11.34	35
C_{66}	24.40	27.39	12

on elastic tensor components for the C–S–H model, suitable for verification purposes in this study. Nevertheless, considering the mentioned reasons, some differences in the mechanical properties are inevitable.

The components of elasticity tensors for the three models are presented in Tables 3–5. It is clear that when the CNT is embedded in the C–S–H phase, the elasticity component in the direction of CNT alignment is strengthened (C_{33} in Table 3 is 36.79, while in Tables 4 and 5 are 148.34 and 153.7, respectively), whereas the other elasticity components are weakened (for example C_{22} in Table 3 is 77 while in Tables 4 and 5 are 43.61 and 30.44, respectively). It means that addition of CNT severely intensifies the "transversely isotropic" response of the CNT-reinforced C–S–H. This is due to the fact that making a hole in the middle section of C–S–H for inserting a CNT, partially disrupts the C–S–H structure and decreases C_{11} and C_{22}. But, the CNT can improve this disruption along its axial axis (C_{33}). This is also true for elastic constants in shear deformation and the principle Young's Modulus.

For easier comparison, the components of the elastic tensors can be condensed into equivalent quasi-isotropic properties. The most common approaches are based on the Voigt, Reuss and Hill methods (more information can be found in [21]). Voigt and Reuss methods calculate the upper and lower bounds for the bulk modulus (K) and shear modulus (G). The mean value of the Voigt and Reuss is called the Voigt–Reuss–Hill (VRH) approximation. After condensing the compliance tensor and calculating the bulk and shear moduli, the isotropic Young's modulus (E) and the Poisson's ratio (v) can be calculated [36]. Table 6 indicates that while it is not expected from the CNT to increase the elastic modulus but it increases the ultimate strength and changes the C–S–H behavior from a brittle Nano-material to a ductile one.

Another way is to inverse the compliance tensor and to determine the elastic tensor $\left(S_{ij} = C_{ij}^{-1}\right)$. The first three diagonal values of the elastic tensor, S_{11}, S_{22}, S_{33}, are the inverse values of the Young's modulus ($E_{ij} = 1/S_{ij}$) in the corresponding X, Y, and Z directions, respectively [21]. The Young's modulus are presented in Table 7, which indicate that addition of CNT to the C–S–H structure significantly increases the elastic modulus along the CNT direction, but has negative influence for the two other directions and decreases them significantly. These results re-confirm the transversely isotropic behavior of this composite material.

The mechanical strength of the models, reported in Table 8, clearly shows that the tensile strength of C–S–H is too weak in the Z direction. Hence, if the CNT is aligned perpendicular to the silicate layer, the most effective properties can be obtained. Nevertheless, there may be a little decline in the tensile and shear strengths along the X and Y directions due to the fact that inserting the CNT weakens the atomic structure of the C–S–H phase, especially the silicate layers. Also, the C–S–H shear strength in the plane of silicate chain (XY) is twice more than the two other planes.

Table 3
Elasticity components for the CSH model.

C_{ij} (Gpa)	X	Y	Z	YZ	XZ	XY
X	76.24	36.16	19.92			
Y		77	24			
Z			36.79			
YZ				9.98		
XZ					11.34	
XY						27.39

Table 4
Elasticity components for the CSH + Armchair model.

C_{ij} (Gpa)	X	Y	Z	YZ	XZ	XY
X	36.75	36.14	14.52			
Y		43.61	17.34			
Z			148.34			
YZ				10.05		
XZ					5.88	
XY						24.92

Table 5
Elasticity components for the CSH + Zigzag model.

C_{ij} (Gpa)	X	Y	Z	YZ	XZ	XY
X	24.87	25.81	17.66			
Y		30.44	17.89			
Z			153.7			
YZ				8.84		
XZ					6.65	
XY						15.41

Table 6
Bulk and shear modulus for C–S–H and CNT-reinforced C–S–H.

Models	Method	K (Gpa)	G (Gpa)	E (Gpa)	v
CSH	Voight	38.89	17.07	44.68	0.31
	Reuss	31.21	14.32	37.25	0.30
	VRH	35.05	15.70	40.97	0.31
CSH + Armchair	Voight	40.83	18.79	48.87	0.30
	Reuss	31.53	5.93	16.74	0.41
	VRH	36.18	12.36	33.29	0.35
CSH + Zigzag	Voight	36.68	16.08	42.08	0.31
	Reuss	43.10	2.34	6.90	0.47
	VRH	39.89	9.21	25.65	0.39

Table 7
Young's modulus for C–S–H and CNT-reinforced C–S–H.

Model No.	Direction	Young's modulus (Gpa)
CSH	X	55.74
	Y	52.73
	Z	28.17
CSH + Armchair	X	6.84
	Y	8.06
	Z	142.26
CSH + Zigzag	X	1.86
	Y	2.76
	Z	138.35

Table 8
Mechanical strength of C–S–H and CNT-reinforced C–S–H.

Models	Direction	Tensile Strength(Gpa)	Compressive Strength (Gpa)	Direction	Shear Strength(Gpa)
CSH	X	3.48	31.33	YZ	1.12
	Y	3.33	40.66	XZ	1.16
	Z	1.58	60.00	XY	2.34
CSH+Armchair	X	2.20	19.50	YZ	0.91
	Y	2.42	31.34	XZ	1.02
	Z	6.71	40.83	XY	1.61
CSH+Zigzag	X	2.11	22.31	YZ	0.97
	Y	2.37	25.57	XZ	0.93
	Z	5.52	36.17	XY	1.68

The tensile stress–strain curves of the models are depicted in Fig. 8. The softening part of the C–S–H curve in tension (Fig. 8a) is very similar to the tensile damage behavior of the cement at the macro scale. As expected, the tensile strength of C–S–H in *X* and *Y* directions decreases when the CNT is embedded. The C–S–H tensile strength along *X* and *Y* directions are 3.48 Gpa and 3.33 Gpa, respectively, while in the *Z* direction is 1.58 Gpa (Table 8). This reduction in *Z* direction in comparison to *X* and *Y* directions is due to the existence of the silicate layers. While embedding the CNT results in around 50% decline in the tensile strength in both *X* and *Y* directions, it increases the tensile strength along the *Z* direction significantly, where a mean value of 6.11 Gpa for the tensile strength is observed for both the zigzag and armchair CNTs (Fig. 8c). This could change the brittle nature of C–S–H material to a ductile response, which sustains larger amount of plastic strain without total degradation. This is important in the cyclic behavior of the macro structures due to absorption of energy and damping of the external forces.

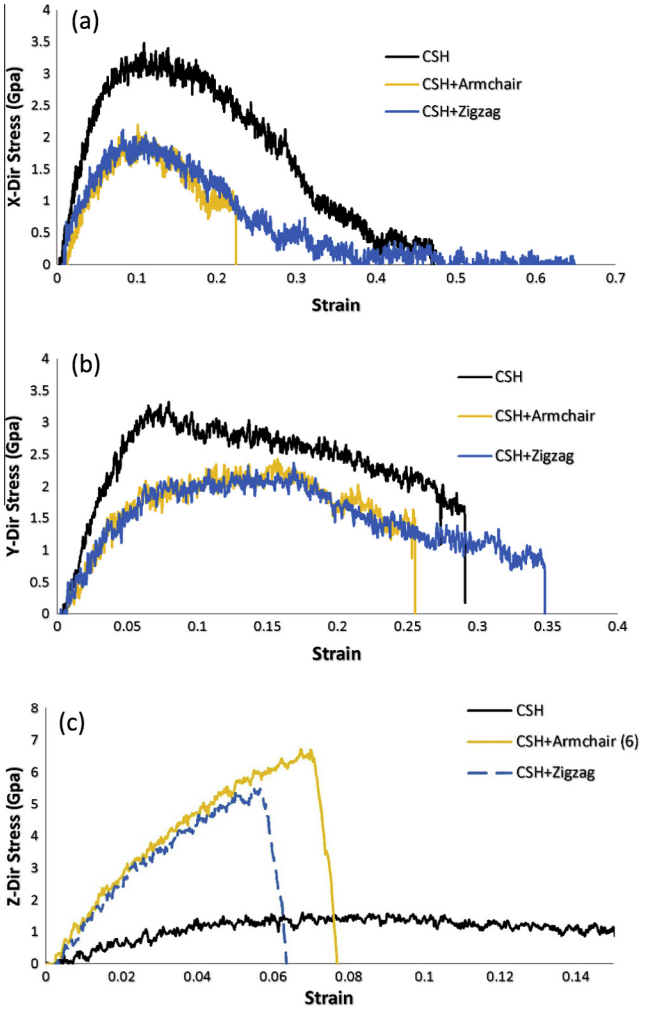

Fig. 8. Tensile stress vs. strain in the (a) *X* direction, (b) *Y* direction and (c) *Z* direction. (For interpretation of the references to colour in this figure legend, the reader is referred to the web version of this article.)

When the tensile force is applied to the overall structure of CNT-reinforced C–S–H in the *Z* direction, the fracture behavior is mainly governed by the strength of CNT. The weakest part of the C–S–H phase in tension is the interlayer between silicate chains where calcium atoms exists, as illustrated in Fig. 9. When the crack in the interlayer of C–S–H appears, the CNT bridges two sides of the crack efficiently and continues to bear the loading until the entire system ruptures.

Making a hole in the middle section of the C–S–H structure, and consequently inserting the CNT in the C–S–H-phase leads to a little decrease in the compressive strength of C–S–H in all directions. The results of compressive strength in *X* and *Y* directions are illustrated in Fig. 10a and b, respectively. The CNT cannot enhance the compressive strength along these directions, because it does not play a reinforcement role along them.

In the *Z* direction, C–S–H can sustain up to 60 Gpa compressive stress. But, the compressive strength of C–S–H reinforced by both armchair and zigzag CNTs are around 38 and 36 Gpa, respectively (Fig. 11). At the first glance, one could predict that the existence of van der Waals interaction between CNT and C–S–H could prevent buckling of CNT in an embedded region. But, the graphical post-processing (Fig. 12) indicates that the weak van der Waals forces among C–S–H and the CNT cannot prevent the local buckling of CNT at larger compressive stresses. Due to the fact that the van der Waals forces between C–S–H and CNT decrease the unbraced length of CNT, the Euler buckling of CNT cannot occur and instead the local-shell buckling mode is dominated. Based on Fig. 11, before buckling of CNT, the CNT-reinforced models could sustain more compressive stress. But, at small compressive strain (around 0.025), CNTs suddenly buckle, resulting in no significant difference between the compressive behavior of all models.

The shear strength of the C–S–H model in the silicate layers plane (*XY* plane) is more than twice the strength in other planes due to the existence of the silicate layers (Fig. 13). Another point, which can be concluded, is that embedding the CNT in the C–S–H medium decreases the shear strength of the model in all directions. This is due to the fact that, based on the classical solid mechanics, the shear strength of a rectangular section depends on the cross section area and inserting a CNT in the hole decreases the shear cross section, disrupt the atomic structure of the silicate layers and consequently, results in lower shear strength. Despite

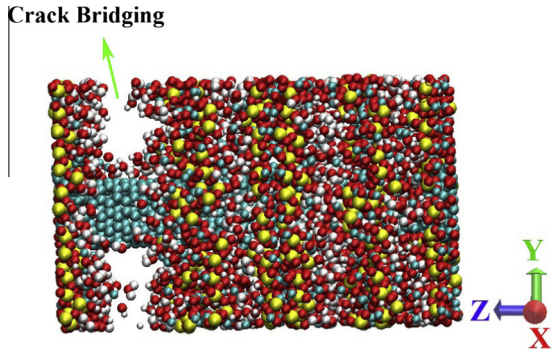

Fig. 9. CNT crack bridging behavior in CNT-reinforced C–S–H. (For interpretation of the references to colour in this figure legend, the reader is referred to the web version of this article.)

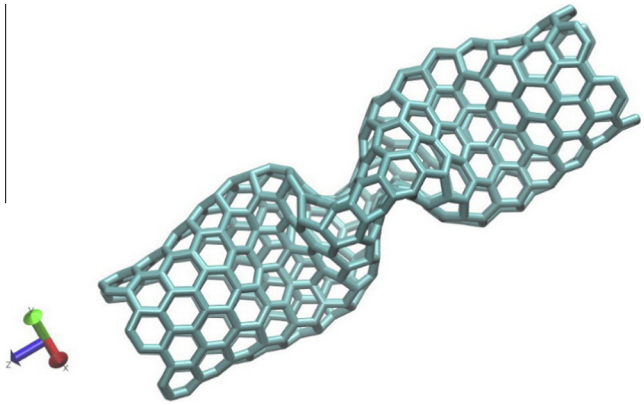

Fig. 12. Local shell buckling of CNT in the C–S–H medium (the C–S–H atoms are removed for clarity). (For interpretation of the references to colour in this figure legend, the reader is referred to the web version of this article.)

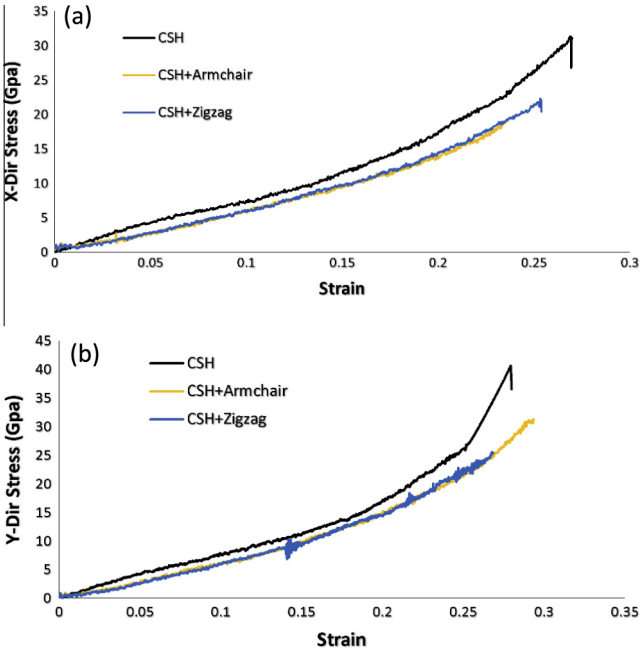

Fig. 10. Compressive stress vs. strain of models in the (a) *X* direction, (b) *Y* direction. (For interpretation of the references to colour in this figure legend, the reader is referred to the web version of this article.)

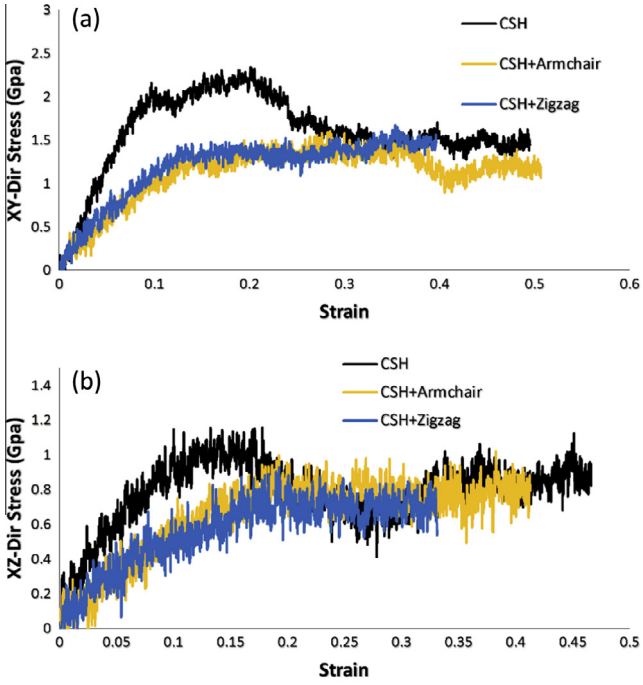

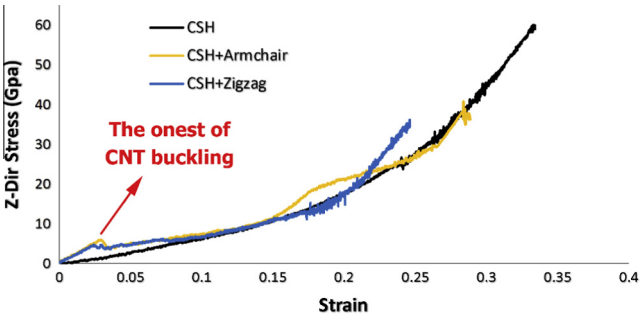

Fig. 11. Compressive stress vs. strain response in the *Z* direction. (For interpretation of the references to colour in this figure legend, the reader is referred to the web version of this article.)

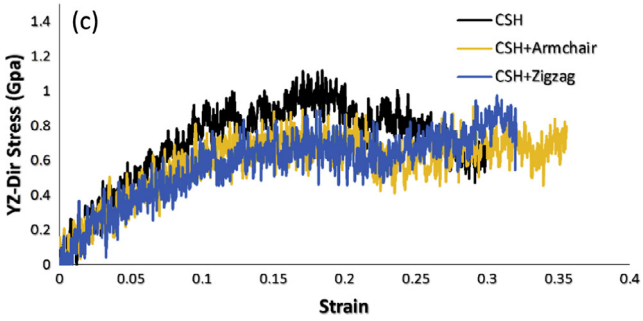

Fig. 13. Shear stress vs. strain response in, (a) *XY* Direction, (b) *XZ* direction, (c) *YZ* direction. (For interpretation of the references to colour in this figure legend, the reader is referred to the web version of this article.)

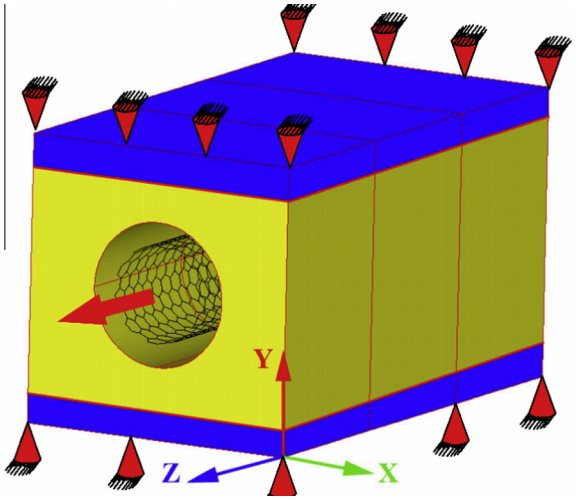

Fig. 14. Boundary conditions of the pull-out model. (For interpretation of the references to colour in this figure legend, the reader is referred to the web version of this article.)

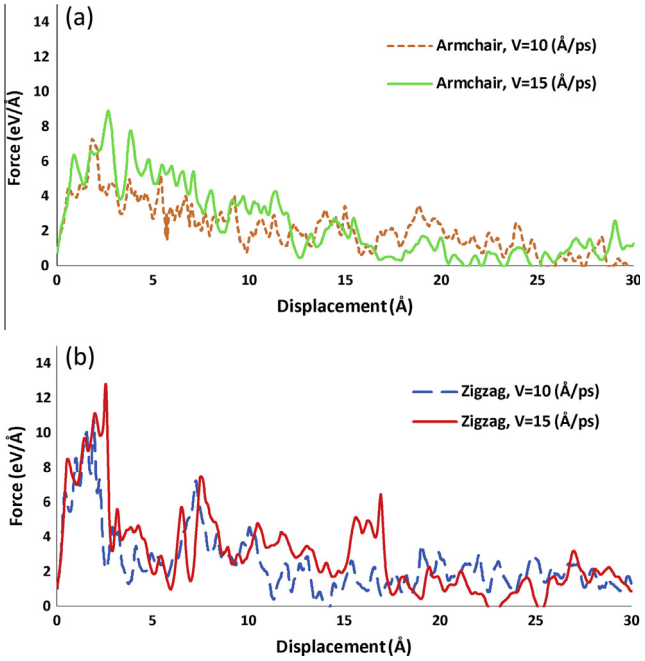

Fig. 15. Pull-out behavior of the models, (a) Armchair CNT, (b) Zigzag CNT. (For interpretation of the references to colour in this figure legend, the reader is referred to the web version of this article.)

the fact that the shear strength of CNT is too high, but its low cross section with respect to C–S–H results in lower overall shear strength of the composite than the pure C–S–H.

5. Interfacial strength and CNT pull-out behavior

The interfacial resistance between the CNT and the surrounding medium is a key factor for the bridging behavior of the CNT-reinforced cement and consequently results in substantial delay in crack opening and propagation. As the bonding between the CNT and C–S–H increases, more CNTs can resist against the crack opening. To find the pull-out behavior of CNT embedded in the cement paste, the armchair and zigzag reinforced C–S–H are analyzed. To find the interfacial strength of the CNT-reinforced C–S–H, 3 Å of the C–S–H is restrained from the top and bottom, as depicted in Fig. 14. Then, a constant velocity in the *Z* direction is applied to the CNT and the resulting interatomic forces between the CNT and C–S–H along the pull-out direction (*Z* direction) are extracted. Yang et al. [37] studied the effect of different velocities on the pull-out behavior of the CNT-reinforced polymeric matrix. In this study, CNTs are subjected to two constant velocities, 10 Å/ps and 15 Å/ps, which are in the order of applied velocities used in [37].

The results of Fig. 15 indicate that the armchair CNT has less interfacial resistance than the zigzag one. In addition, the pull-out velocity can increase the interfacial strength of CNTs, which means that under dynamic loadings such as impact and explosion, CNTs are expected to be more efficient than in the static condition. The overall behavior of the pull-out can be estimated by a bilinear trend: an increasing path with a positive slope to reach the peak strength, which will then be degraded to zero with a negative slope. The peak interfacial resisting force at the 15 Å/ps pull-out speed for the armchair CNT is 8.9 eV/Å, while this value for the zigzag CNT is 12.82 eV/Å. After the peak point, the interfacial resisting force of the zigzag CNT is degraded at a much slower pace than the armchair.

6. Conclusion

In this work, mechanical properties of the CNT-reinforced C–S–H are evaluated by means of the molecular dynamics simulation. The results indicate that the properties of C–S–H are very similar to the transversely isotropic material due to the existence of silicate layers. Addition of CNT can substantially intensify the transversely isotropic response of the CNT-reinforced C–S–H. Nevertheless, embedding the CNT increases the tensile strength along the *Z* direction up to 6 Gpa and allows for the bridging effect on the two sides of the crack efficiently. This could change the brittle nature of C–S–H material to a ductile response which sustains larger amount of the plastic strain. For the compressive behavior,

Table A-1
Lennard-Jones potential parameters for C–S–H.

Atom i	Atom j	ε (eV Å)	σ (Å)	Atom *i*	Atom *j*	ε (eV Å)	σ (Å)
Ca	O	3.76843E−05	4.365	Oh	Oh	2.67997E−03	3.447
Ca	Ob	3.06158E−05	5.452	Ob	O	1.96878E−03	3.625
Ca	Oh	3.76843E−05	4.365	O	Oh	1.96878E−03	3.625
Cw	O	6.33131E−05	4.365	Ob	Oh	2.67997E−03	3.447
Cw	Ob	4.50997E−05	4.445	Ca	Ow	3.79879E−05	4.365
Cw	Oh	4.50997E−05	4.445	Cw	Ow	2.61925E−05	4.472
Si	O	2.42845E−05	3.269	O	Ow	2.28101E−04	4.240
Si	Ob	2.58023E−05	3.260	Ow	Ob	3.78144E−02	2.895
Si	Oh	2.58023E−05	3.260	Oh	Ow	3.78144E−02	2.895
O	O	5.37728E−02	2.735	Ow	Ow	6.67823E−03	3.162
Ob	Ob	2.67997E−03	3.447				

Table A-2
Lennard-Jones potential parameters between CSH and the CNT.

Atom *i*	Atom *j*	ε (eV Å)	σ (Å)	Atom *i*	Atom *j*	ε (eV Å)	σ (Å)
Si	C	1.38095E−05	3.351	Ob	C	4.01324E−03	3.282
Ca	C	2.28325E−05	4.480	O	C	4.01324E−03	3.282
Cw	C	2.28325E−05	4.480	Oh	C	4.01324E−03	3.282
Ow	C	4.01324E−03	3.282				

the local-shell buckling mode is dominated for the CNT and no significant difference between the compressive behavior of all models is observed. The shear strength of the C–S–H model in the plane of silicate layers is more than twice the strength in other planes due to the existence of the silicate layers. Furthermore, embedding the CNT in the C–S–H medium decreases the shear strength of the model in all directions. The armchair CNT has less interfacial resistance than the zigzag one in the C–S–H medium.

Acknowledgement

The technical support of the High Performance Computing Lab, School of Civil Engineering, University of Tehran is acknowledged. The financial support of Iran Nanotechnology Initiative Council is appreciated. The help and useful discussions with Dr. Mohammad Javad Abdolhosseini Qomi at University of California, Irvine and Dr. Roland J.-M. Pellenq at Massachusetts Institute of Technology are gratefully acknowledged. Also, the support of Iran National Science Foundation is gratefully appreciated.

Appendix A

See Tables A-1 and A-2.

References

[1] Eftekhari M, Mohammadi S. Multiscale dynamic fracture behavior of the carbon nanotube reinforced concrete under impact loading. Int J Impact Eng 2016;87:55–64.
[2] Eftekhari M, Hatefi Ardakani S, Mohammadi S. An XFEM multiscale approach for fracture analysis of carbon nanotube reinforced concrete. Theoret Appl Fract Mech 2014;72:64–75.
[3] Eftekhari M, Mohammadi S, Khoei AR. Effect of defects on the local shell buckling and post-buckling behavior of single and multi-walled carbon nanotubes. Comput Mater Sci 2013;79:736–44.
[4] Griebel M, Hamaekers J. Molecular dynamics simulations of the elastic moduli of polymer–carbon nanotube composites. Comput Methods Appl Mech Eng 2004;193(17–20):1773–88.
[5] Allen AJ, Thomas JJ, Jennings HM. Composition and density of nanoscale calcium–silicate–hydrate in cement. Nat Mater 2007;6(4):311–6.
[6] Cwirzen A, Habermehl-Cwirzen K, Penttala V. Surface decoration of carbon nanotubes and mechanical properties of cement/carbon nanotube composites. Adv Cem Res 2008;20(2):65–73.
[7] Musso S, Tulliani J-M, Ferro G, Tagliaferro A. Influence of carbon nanotubes structure on the mechanical behavior of cement composites. Compos Sci Technol 2009;69(11–12):1985–90.
[8] Vorel J, Šmilauer V, Bittnar Z. Multiscale simulations of concrete mechanical tests. J Comput Appl Math 2012;236(18):4882–92.
[9] Ji Q, Pellenq RJM, Van Vliet KJ. Comparison of computational water models for simulation of calcium–silicate–hydrate. Comput Mater Sci 2012;53(1):234–40.
[10] Bauchy M, Abdolhosseini Qomi MJ, Bichara C, Ulm F-J, Pellenq RJM. Nanoscale structure of cement: viewpoint of rigidity theory. J Phys Chem C 2014;118(23):12485–93.
[11] Bauchy M, Qomi MJA, Ulm F-J, Pellenq RJ-M. Order and disorder in calcium–silicate–hydrate. J Chem Phys 2014;140(21):214503.
[12] Qomi MJA, Bauchy M, Ulm F-J, Pellenq RJ-M. Anomalous composition-dependent dynamics of nanoconfined water in the interlayer of disordered calcium-silicates. J Chem Phys 2014;140(5):054515.
[13] Powers TC, Brownyard TL. Studies of the physical properties of hardened Portland cement paste. J Proc 1946;43(9).
[14] Taylor HFW. Proposed structure for calcium silicate hydrate gel. J Am Ceram Soc 1986;69(6):464–7.
[15] Tennis PD, Jennings HM. A model for two types of calcium silicate hydrate in the microstructure of Portland cement pastes. Cem Concr Res 2000;30(6):855–63.
[16] Abdolhosseini Qomi MJ, Krakowiak KJ, Bauchy M, Stewart KL, Shahsavari R, Jagannathan D, et al. Combinatorial molecular optimization of cement hydrates. Nat Commun 2014:5.
[17] Manzano H, Moeini S, Marinelli F, van Duin ACT, Ulm F-J, Pellenq RJM. Confined water dissociation in microporous defective silicates: mechanism, dipole distribution, and impact on substrate properties. J Am Chem Soc 2012;134(4):2208–15.
[18] Manzano H, Dolado J, Guerrero A, Ayuela A. Mechanical properties of crystalline calcium-silicate-hydrates: comparison with cementitious C–S–H gels. Phys Status Solidi (a) 2007;204(6):1775–80.
[19] Pellenq RJ-M, Kushima A, Shahsavari R, Van Vliet KJ, Buehler MJ, Yip S, et al. A realistic molecular model of cement hydrates. Proc Natl Acad Sci 2009;106(38):16102–7.
[20] Murray SJ, Subramani VJ, Selvam RP, Hall KD. Molecular dynamics to understand the mechanical behavior of cement paste. Trans Res Rec: J Transport Res Board 2010;2142(1):75–82.
[21] Shahsavari R, Pellenq RJ-M, Ulm F-J. Empirical force fields for complex hydrated calcio-silicate layered materials. Phys Chem Chem Phys 2011;13(3):1002–11.
[22] Abdolhosseini Qomi MJ, Ulm F-J, Pellenq RJ-M. Evidence on the dual nature of aluminum in the calcium–silicate–hydrates based on atomistic simulations. J Am Ceram Soc 2012;95(3):1128–37.
[23] Bauchy M, Laubie H, Abdolhosseini Qomi MJ, Hoover CG, Ulm FJ, Pellenq RJM. Fracture toughness of calcium–silicate–hydrate from molecular dynamics simulations. J Non-Cryst Solids 2015;419(0):58–64.
[24] Abdolhosseini Qomi MJ, Ulm F-J, Pellenq RJM. Physical origins of thermal properties of cement paste. Phys Rev Appl 2015;3(6):064010.
[25] Manzano H, Durgun E, Abdolhosseine Qomi MJ, Ulm F-J, Pellenq RJM, Grossman JC. Impact of chemical impurities on the crystalline cement clinker phases determined by atomistic simulations. Cryst Growth Des 2011;11(7):2964–72.
[26] Qomi M, Bauchy M, Ulm F-J, Pellenq R. Polymorphism and its implications on structure-property correlation in calcium–silicate–hydrates. In: Sobolev K, Shah SP, editors. Nanotechnology in construction. Springer International Publishing; 2015. p. 99–108.
[27] Erik TT, Tsu-Wei C. Aligned multi-walled carbon nanotube-reinforced composites: processing and mechanical characterization. J Phys D Appl Phys 2002;35(16):L77.
[28] Xia ZH, Lou J, Curtin WA. A multiscale experiment on the tribological behavior of aligned carbon nanotube/ceramic composites. Scripta Mater 2008;58(3):223–6.
[29] Plimpton S. Fast parallel algorithms for short-range molecular dynamics. J Comput Phys 1995;117(1):1–19.
[30] Wolf D, Keblinski P, Phillpot S, Eggebrecht J. Exact method for the simulation of Coulombic systems by spherically truncated, pairwise r−1 summation. J Chem Phys 1999;110(17):8254–82.
[31] Tersoff J. Modeling solid-state chemistry: interatomic potentials for multicomponent systems. Phys Rev B 1989;39(8):5566–8.
[32] Sanchez F, Zhang L. Molecular dynamics modeling of the interface between surface functionalized graphitic structures and calcium–silicate–hydrate: Interaction energies, structure, and dynamics. J Colloid Interface Sci 2008;323(2):349–58.
[33] Sanchez F, Zhang L. Interaction energies, structure, and dynamics at functionalized graphitic structure–liquid phase interfaces in an aqueous calcium sulfate solution by molecular dynamics simulation. Carbon 2010;48(4):1210–23.
[34] Khoei AR, Ban E, Banihashemi P, Abdolhosseini Qomi MJ. Effects of temperature and torsion speed on torsional properties of single-walled carbon nanotubes. Mater Sci Eng, C 2011;31(2):452–7.
[35] Richardson IG. The nature of C–S–H in hardened cements. Cem Concr Res 1999;29(8):1131–47.
[36] Puertas F, Palacios M, Manzano H, Dolado J, Rico A, Rodríguez J. A model for the CASH gel formed in alkali-activated slag cements. J Eur Ceram Soc 2011;31(12):2043–56.
[37] Yang L, Tong L, He X. MD simulation of carbon nanotube pullout behavior and its use in determining mode I delamination toughness. Comput Mater Sci 2012;55:356–64.